Simultaneous Optimization of the Airframe, Powerplant, and Operation of Transport Aircraft

Mark Drela
MIT Department of Aeronautics and Astronautics
Cambridge, Massachusetts, USA

Abstract

Global optimization of transport aircraft is performed to minimize fuel burn for a specified mission. The design space includes the geometry, wing airfoils, primary structure, engine size and cycle parameters, and the flight profile parameters. The method employs a number of physics-based models for structural sizing and weight estimation, viscous CFD for all major aerodynamic components, and a component-based turbofan simulation. The models drive a trajectory integration to calculate mission fuel burn. These physics-based models mostly eliminate the reliance on historical weight and engine performance correlations and wetted-area drag prediction methods, and hence give confidence for development of radical transport aircraft which fall outside of historical trends.

Computed examples show a D8.x aircraft series to replace the Boeing 737-800, with up to 49% less fuel burn using today's alumimum technology, and up to 71% less fuel burn using year 2030 forecast technology. These exploit a novel fuselage configuration via its indirect effects on structural weight, lift to drag ratio, and propulsive efficiency, all captured by the collection of coupled low-order models. Sensitivity of the fuel burn to cruise Mach number change, materials allowables improvements, and span constraints is also investigated.

1 Introduction

1.1 Background

There is a vast body of work on conceptual and preliminary aircraft design. The more traditional approaches of e.g. Roskam [1], Torrenbeek [2], Raymer [3], have relied heavily on historical weight correlations, drag build-ups based on wetted area and form-factor accounting, and tabulated engine performance data for their design evaluations. The ACSYNT program [4],[5] likewise relies on such models, with a more detailed treatment of the geometry. More recently, optimization-based approaches such as those of Knapp [6], the WINGMOD code of Wakayama [7],[8], and in particular the PASS program of Kroo [9] perform tradeoffs in a much more detailed geometry parameter space, but still rely on simple drag and engine performance models. Finally, extensive work, e.g. Martins et al [10], has been done for optimization of high-fidelity coupled aerodynamic plus structural models, but these also do not address the engine and mission parameters in detail, and are typically much better suited for later design-refinement stages rather than the early conceptual design stage which is the focus of the present work.

1.2 Motivation

The recent advent of turbofan engines with extremely high bypass ratios (Pratt geared turbofan), advanced composite materials (Boeing 787), and possibly less restrictive operational restrictions (Free-Flight ATC concept), make it of great interest to re-examine the overall aircraft/engine/operation system to maximize transportation efficiency. In addition, greater emphasis on limiting noise and emissions dictates that such aircraft design examination be done under possibly stringent environmental constraints.

It is arguable that current transport aircraft characteristics (Mach, sweep, cabin layout, etc) and engine characteristics (pressure ratios, bypass ratio, turbine inlet temperatures) have evolved from the early DH Comet and B-707 aircraft and turbojets by local optimization within each discipline. This is sketched in Fig. 1, and there's significant evidence to be presented here that a global optimum exists outside of current practice offering very large fuel burn savings over today's aircraft, even with minimal technology improvement.

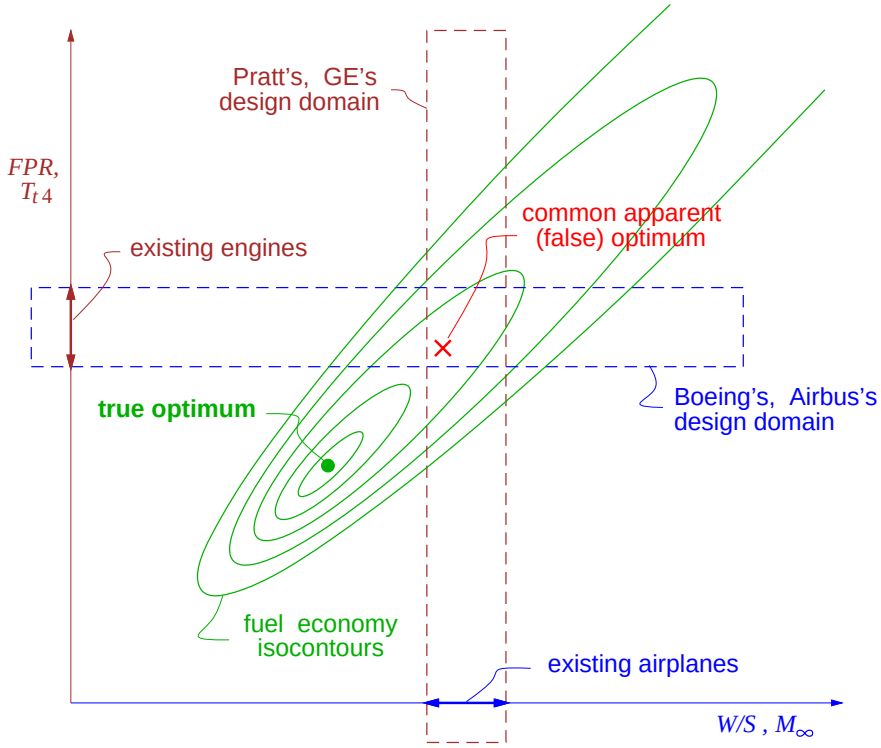

Figure 1: Domain-restricted optimum and true global optimum.

The present work was performed in response to the NASA N+3 program to develop technology for future air transport aircraft for years 2030-2035, with goals of reducing fuel burn by 70%, emissions by 75%, and noise by 71 dB. The present work will focus entirely on fuel burn reduction, as this was deemed to be the driving challenge.

1.3 TASOPT Approach

To examine and evaluate future aircraft with potentially unprecedented airframe, aerodynamic, engine, or operation parameters, it is desirable to dispense with as many of the historically-

based methods as possible, since these cannot be relied on outside of their data-fit ranges. The approach developed here and implemented in program TASOPT (**T**ransport **A**ircraft **S**ystem **OPT**imization) is to dispense with such historical approaches, and instead rely on low-order physical models implementing fundamental structural, aerodynamic, and thermodynamic theory and associated computational methods for all primary predictions. Historical correlations are used only where absolutely necessary, and in particular only for some of the secondary structure and for aircraft equipment. Modeling the bulk of the aircraft structure, aerodynamics, and propulsion by fundamentals gives considerable confidence that the resulting optimized design is realizable, and not some artifact of inappropriate extrapolated data fits.

2 Structural and Weight Models

The assumed weight breakdown is diagrammed in Fig. 2, and also indicates the degree of airframe detail treated by TASOPT.

The airframe primary structure elements are modeled as simplified geometric shapes, with the gauge-sizing loads for each element imposed at the critical loading cases listed in Table 1.

Table 1: Load cases for sizing primary structural elements

Max $N_{\text{lift}} W_{\text{MTO}}$:	wing bending spar caps and shear webs
Max Δp at $h_{\max}$:	fuselage skin tension
Max L_{vtail} at V_{NE}:	fuse and tailcone skin shear, added side stringers, tail caps and webs
Max L_{htail} at V_{NE}:	added top/bottom stringers, tail caps and webs
Max $N_{\text{land}} W_{\text{MTO}}$:	added top/bottom stringers, fuselage floor beams

2.1 Fuselage

The fuselage, as sketched in Fig. 3, is assumed to be a pressure vessel with spherical or ellipsoidal endcaps, which is also subjected to bending and torsion loads at the various loading scenarios considered.

The fuselage cross-section, shown in Fig. 4, has a "double-bubble" cross-section which reduces to the usual simple circular cross section for the zero bubble offset width $w_{\text{db}} = 0$ case. The skin and added assumed stringers and frames are all sized to obtain a specified stress at the specified load situations. A payload-loading analysis provides the weight of the floor. All other secondary-structure weights and interior furnishings (windows, doors, seats, insulation, galleys, etc.) are estimated using historical weight fractions, and are assumed to be proportional to the number of passengers, or interior area, or cabin length, as appropriate for each element.

2.2 Wing

The wing, shown in Fig. 5, is assumed to have a double piecewise linear taper planform at some sweep angle, and is subjected to a double piecewise linear aerodynamic lift distribution with

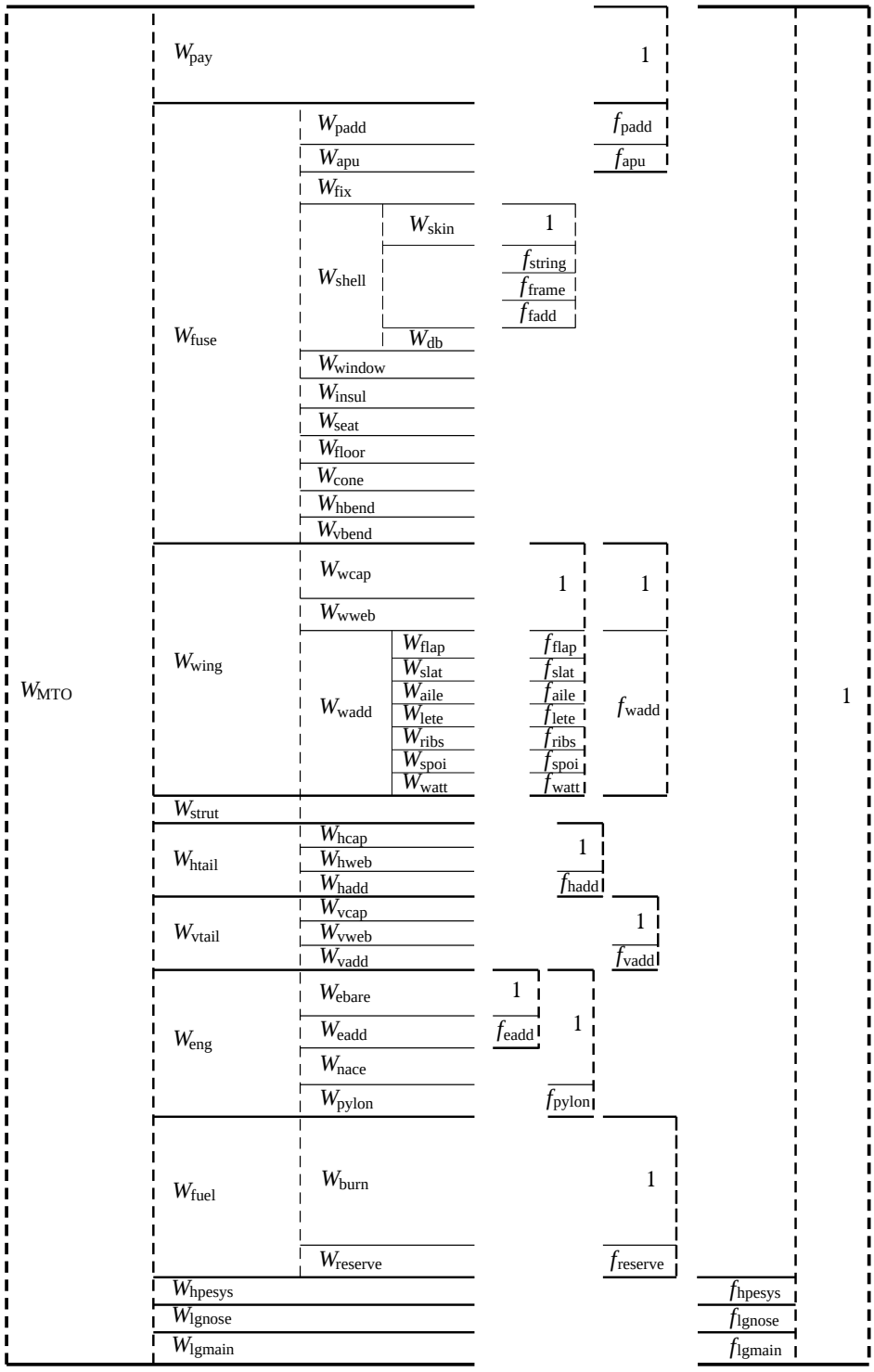

Figure 2: Aircraft weights and weight fractions breakdown.

tip and fuselage-carryover lift modifications. Relieving distributed weight loads of the structure and fuel are also imposed. An optional strut or engine with its structural or relieving weight load is also assumed to act at the planform break as sketched.

The wing cross-section, shown in Fig. 6, consists of a structural box with curved top and bottom sparcaps, with front and rear shear webs. These elements are sized to achieve specified

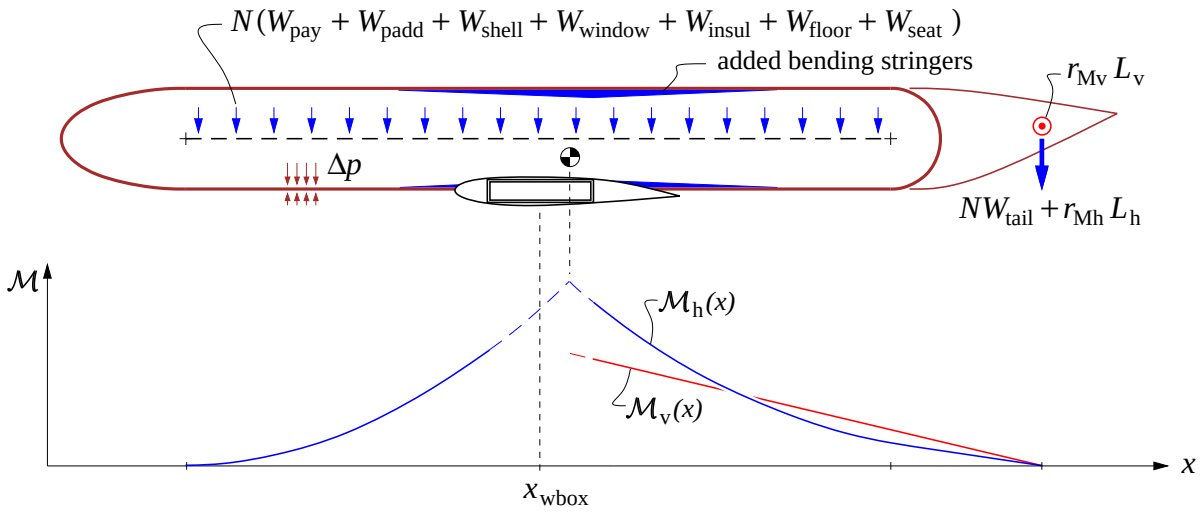

Figure 3: Fuselage layout, pressure load, and bending load.

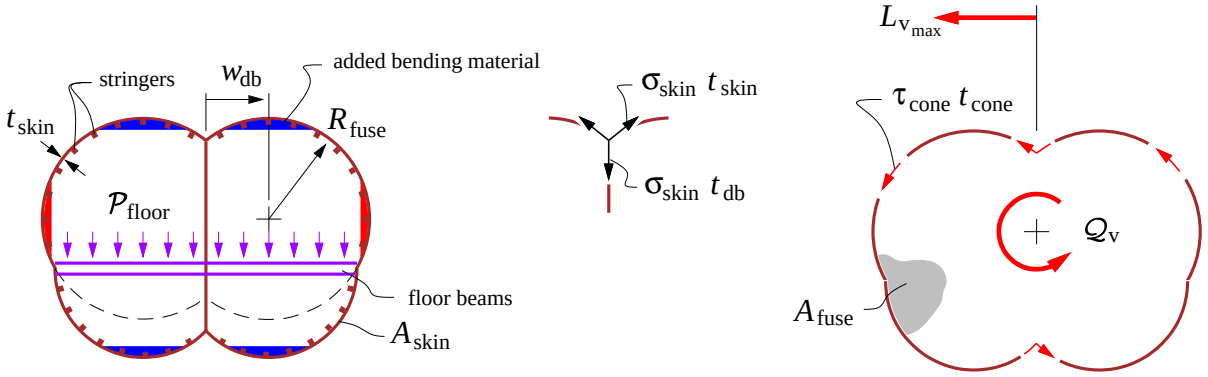

Figure 4: Fuselage cross-section, shell/web junction tension flows, and torsion shear flow from vertical tail load. Fuselage frames are not shown.

allowable stresses due to the perpendicular-plane bending moment $\mathcal{M}_\perp$ at the chosen critical loading condition at a maximum allowable load factor. The known structural gauges then give the wing's primary structural weight and weight moments. The internal box volume also gives the maximum fuel capacity and fuel weight. The weight of the slats, flaps, ailerons, spoilers, and other secondary structure is currently estimated using historical weight fractions.

2.3 Tail Surfaces

The tail surfaces are treated using the same model as for the wing, except that struts, engines, and fuel are assumed absent in the code implentation. Also, the sizing load case is different as given in Table 1.

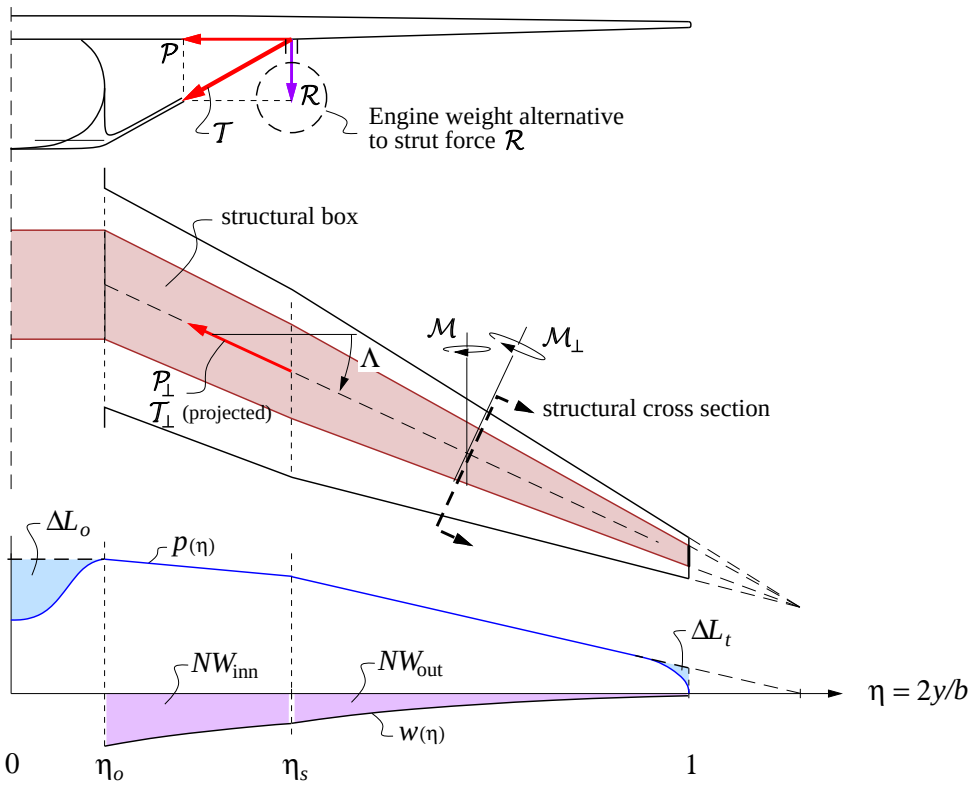

Figure 5: Wing planform and applied aerodynamic and weight loads. An optional strut or engine can also impose added structural or weight loads.

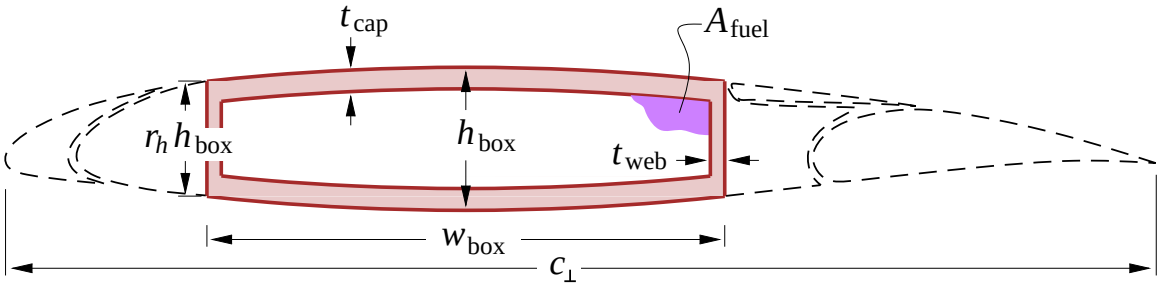

Figure 6: Wing or tail airfoil and structure cross-section, shown perpendicular to spar axis. Leading edges, fairings, slats, flaps, and spoilers contribute to weight but not to the primary structure.

2.4 Engine Weights

The engine weight is predicted by the following empirical relation.

$$W_{eng} = \left(\frac{\dot{m}_{core}}{\dot{m}_{ref}}\right)^{b_0} \left[W_0 + W_{fan}\left(\frac{BPR}{BPR_{ref}}\right)^{b_1} + W_{case}\left(\frac{OPR}{OPR_{ref}}\right)^{b_2}\right] \quad (1)$$

The three terms in the brackets represent the weights of the core spool, the fan spool which scales with the bypass ratio BPR, and the casing which scales with the overall pressure ratio OPR, all scaled by the core mass flow $\dot{m}_{core}$. The coefficients and exponents in the weight model are calibrated by nonlinear regression using weights of a large number of existing engines, and

fits the weights to within about ±5% for all the modern turbofan engines examined, from the JT15D (2000 lb thrust) to the GE90 (90000 lb thrust). The exponents b_0, b_2 thus determined are roughly unity, while b_1 is somewhat greater than unity which reflects the manifestation of the cube-square law in the fan weight.

3 Aerodynamic Models

TASOPT uses viscous/inviscid CFD methods to predict the drag of the wing airfoils, fuselage, and tail surfaces. The more traditional wetted-area drag prediction techniques are *not* used, since these typically involve ad-hoc form factor corrections based on historical correlations with assumed shapes, and hence would be of questionable validity for the novel D8.x fuselage shape presented later.

A key feature of the D8.x aircraft is Boundary Layer Ingestion (BLI). The necessary force and power accounting involves both the aerodynamic models and also the engine models to be presented later. The details are based on the Power Balance approach of Drela [11], and for brevity will not be given here.

3.1 Wing profile lift and profile drag

The wing airfoil performance is represented by a parameterized transonic airfoil family spanning a range of thicknesses, shown in Fig. 7. Each airfoil has been designed and optimized for good

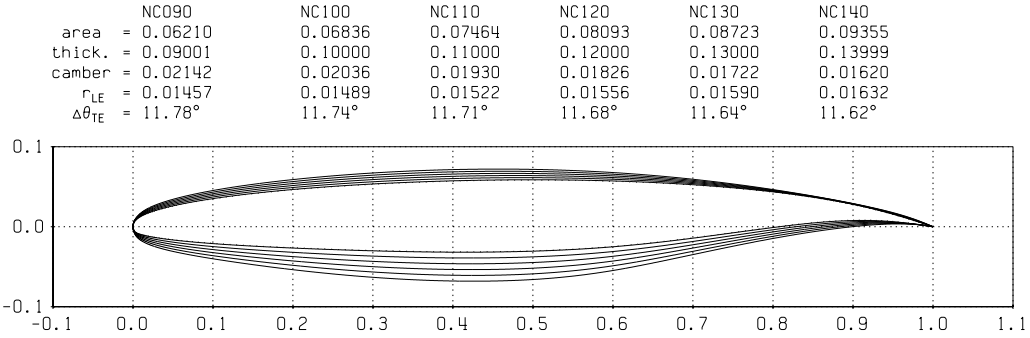

Figure 7: Airfoil family used to generate airfoil-performance database.

transonic drag rise behavior, which was determined by the 2D viscous/inviscid MSES code [12] for a range of lift coefficients and Mach numbers. A Reynolds number correction is also applied. The result is a 2D airfoil performance database which provides the section profile drag as a function of the section lift coefficient, wing-normal Mach, thickness ratio, and chord Reynolds number.

$$c_d = \mathcal{F}\left(c_\ell, M_\perp, \tfrac{t}{c}, Re_c\right) \tag{2}$$

This is integrated along the wing using standard corrections for the wing sweep angle Λ, and modified to account for shock unsweeping at wing root, as sketched in Fig. 8. The overall wing profile drag model then has the form

$$C_{D_{\text{wing}}} = \mathcal{F}\left(C_L, M_\infty, \Lambda, \tfrac{t}{c}, Re_c\right) \tag{3}$$

and gives reliable transonic lift and drag performance predictions of the entire wing in cruise, and also in high climb and high descent.

This airfoil parameterization in effect represents an arbitrary "rubber airfoil", whose thickness can now be optimized by trading profile drag versus structural merit, together with all the other airframe, engine, and operating variables. It also has the advantage of eliminating the need for empirical wave drag estimates, since the wave drag has been captured by the viscous CFD calculations and hence is implicitly contained in the airfoil performance database.

2D multielement MSES calculations were also used to estimate the airfoils' and hence the wing's $C_{L_{\max}}$ and profile drag for the flaps-down case, for takeoff distance predictions. The airfoil thickness is assumed to have a negligible effect here, so the coefficients can be computed offline and another airfoil database for runtime execution is not required.

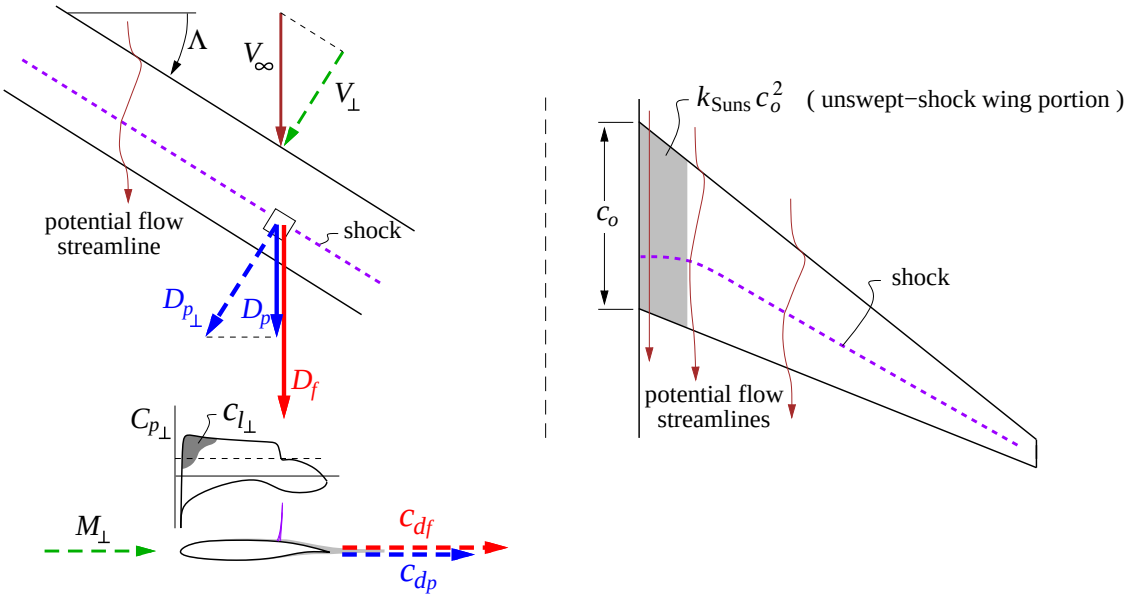

Figure 8: Application of 2D airfoil c_d and c_ℓ to an infinite swept wing, with wing root correction to account for local shock unsweep roughly over the area $k_{\text{uns}} c_o^2$.

3.2 Fuselage profile drag

As for the wing airfoils, the fuselage drag is also obtained from compressible viscous/inviscid CFD. The fuselage's potential flow is represented by a compressible source line or source strip, whose strengths are determined from the fuselage's cross-sectional area distribution $A_{(x)}$, as shown in Fig. 9. The potential flow is then used together with the perimeter distribution $b_{0(x)}$ in an XFOIL-type [13] viscous/inviscid coupling scheme to compute the viscous flow, and in particular the displacement, momentum, and kinetic energy area distributions $\Delta^*{}_{(x)}$, $\Theta_{(x)}$, $\Theta^*{}_{(x)}$. The downstream wake momentum area then gives the fuselage profile drag.

$$C_{D_{\text{fuse}}} \;=\; \frac{2\Theta_{\text{wake}}}{S} \;=\; \mathcal{F}\left(A_{(x)}, b_{0(x)}, M_\infty, Re_l\right) \tag{4}$$

Correlations for effective fineness ratio, tailcone closure angles, etc. which are used by wetted-area methods are not needed here, so that this approach is well suited for the unusual D8.x fuselage shape presented later.

The present approach also provides the kinetic energy thickness Θ^* at the engine-inlet location, which is needed for an accurate thrust and power accounting of BLI. This engine-inlet flow state information would not be immediately available from traditional wetted-area drag prediction methods.

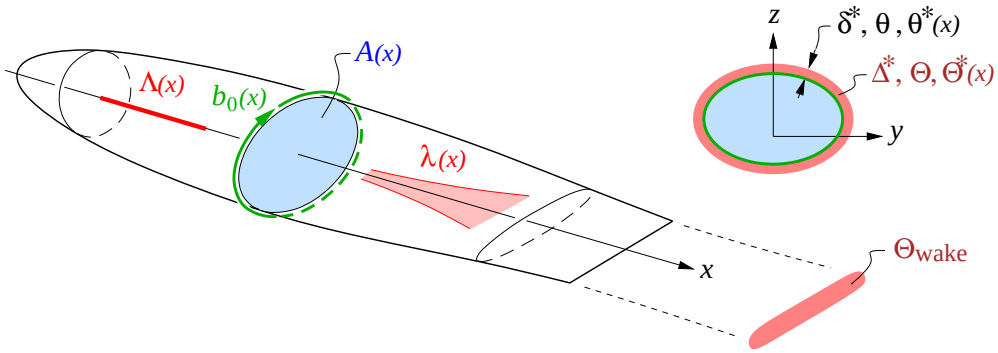

Figure 9: Boundary layer evolution and fuselage drag prediction by viscous/inviscid calculation, driven by the fuselage's cross-sectional area $A_{(x)}$ and perimiter $b_{0(x)}$ distributions.

3.3 Nacelle profile drag

The drag contribution of the exterior of the engine nacelle is estimated using the turbulent flat-plate $C_f(Re_l)$ law together with an estimated surface velocity distribution in a dissipated-power relation.

$$C_{D_{\text{nace}}} = \frac{1}{S} \iint C_f \left(\frac{V}{V_\infty}\right)^3 dA \tag{5}$$

The surface velocity V distribution is estimated from the flight and fan-face Mach numbers, as sketched in Fig. 10. This approach makes the predicted nacelle drag strongly dependent on the flight speed and the engine power setting as is the case in reality, and thus provides realistic nacelle drag estimates over the entire flight regime.

3.4 Vortex drag

Overall aircraft vortex (or induced) drag is predicted by the standard Trefftz-Plane drag integral,

$$C_{D_i} = \frac{1}{V_\infty^2 S} \int \Gamma \, w_n \, ds' \tag{6}$$

with the circulation in the Trefftz Plane tied directly to the spanwise wing aero load distribution.

$$\Gamma_{(y')} = \frac{p_{(y)}}{\rho V_\infty} \tag{7}$$

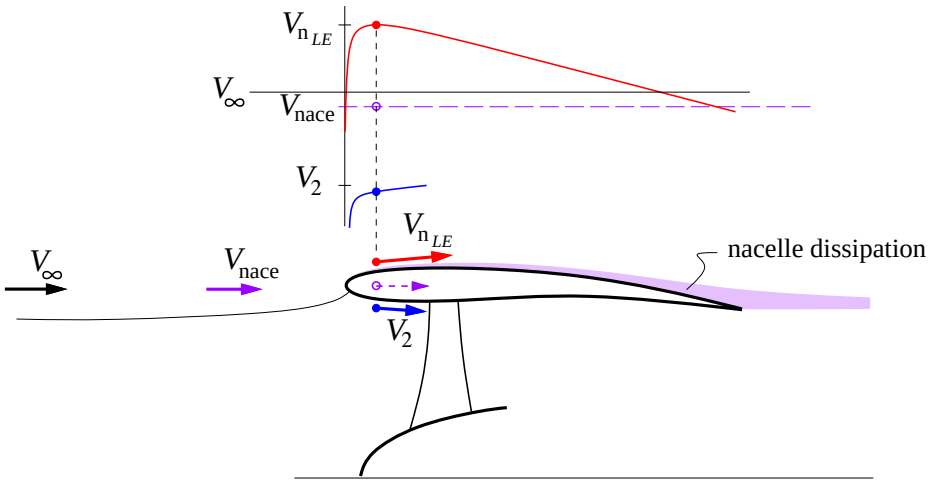

Figure 10: Velocity distribution on inside and outside of engine nacelle. Outside velocity determines nacelle dissipation and implied nacelle drag. The $V_{n_{LE}} > V_2$ case shown is for a typical cruise condition, while $V_{n_{LE}} < V_2$ will occur at low speeds and high power.

The relation between the wake and wing locations y' and y connected by a streamline uses mass conservation applied to streamtubes inside y' and y, sketched in Fig. 11. This accounts for the wake contraction and resulting induced drag penalty due to the fuselage. The tail wake and its load are obtained from a longitudinal trim balance analysis, and are also included in the Trefftz Plane calculation. This then captures trim drag, and together with the structural weight models enables spanload shape optimization.

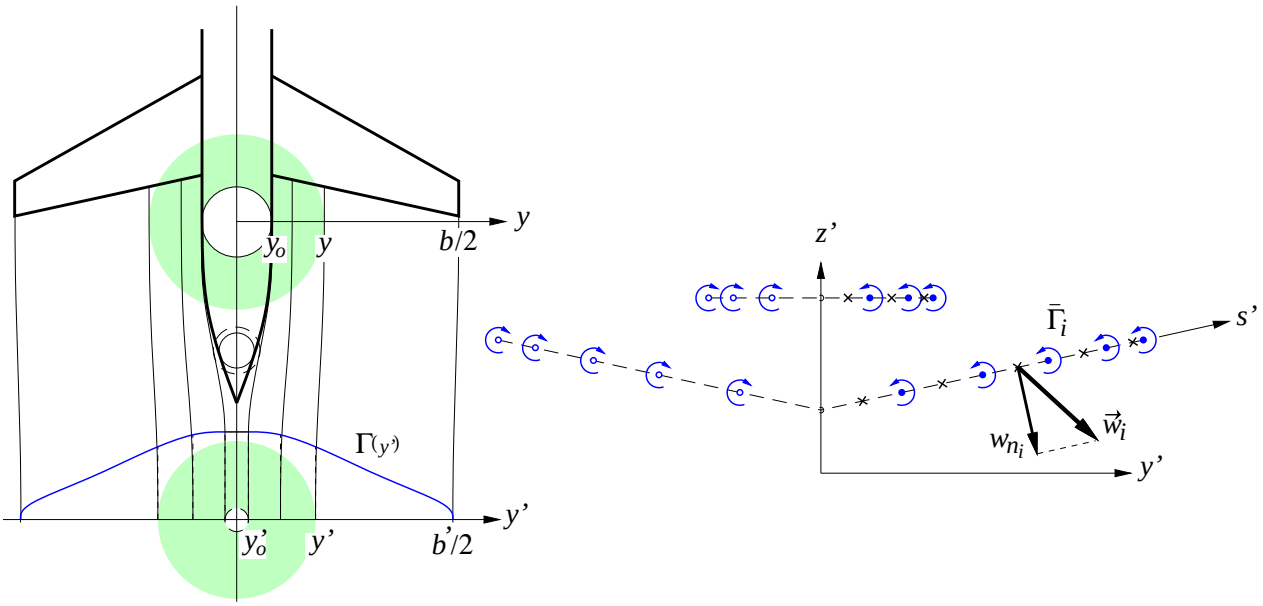

Figure 11: Wake streamline contraction due to fuselage thickness carries wing circulation into the wake, which is then used in the Trefftz-Plane impulse and kinetic energy calculation. The wake of the loaded horizontal tail is also included, thus capturing trim drag.

4 Engine Performance Model

TASOPT uses a fairly detailed component-based turbofan model, sketched in Fig. 12. It is based on the approach of Kerrebrock [14], with added models for turbine cooling flow and cooling loss predictions. Variable $c_{p(T)}$ effects using constituent-based gas properties are also used to allow treating almost any common hydrocarbon or alcohol fuel without the need to estimate and input effective c_p's in the flowpath. The overall engine model code implentation has a design mode which is used to size the engine flow areas for cruise, given a specified thrust $F_{\rm eng}$, turbine inlet temperature T_{t4}, design fan and overall pressure ratios $FPR_{\rm D}, OPR_{\rm D}$, design bypass ratio $BPR_{\rm D}$, the flight conditions, and the BLI inlet kinetic energy defect $K_{\rm inl}$.

$$[A_{\rm fan}, A_{\rm comp\cdots}] \;=\; \mathcal{F}\,(F_{\rm eng}, T_{t4}, FPR_{\rm D}, OPR_{\rm D}, BPR_{\rm D\cdots}; M_\infty, p_\infty, T_\infty, K_{\rm inl\cdots}) \tag{8}$$

With the flow areas fixed, the same model is also cast in an off-design mode which is used to determine performance at takeoff, climb, and descent.

$$[F_{\rm eng}, TSFC, FPR, OPR, BPR\cdots] \;=\; \mathcal{F}\,(T_{t4}, A_{\rm fan}, A_{\rm comp\cdots}; M_\infty, p_\infty, T_\infty, K_{\rm inl\cdots}) \tag{9}$$

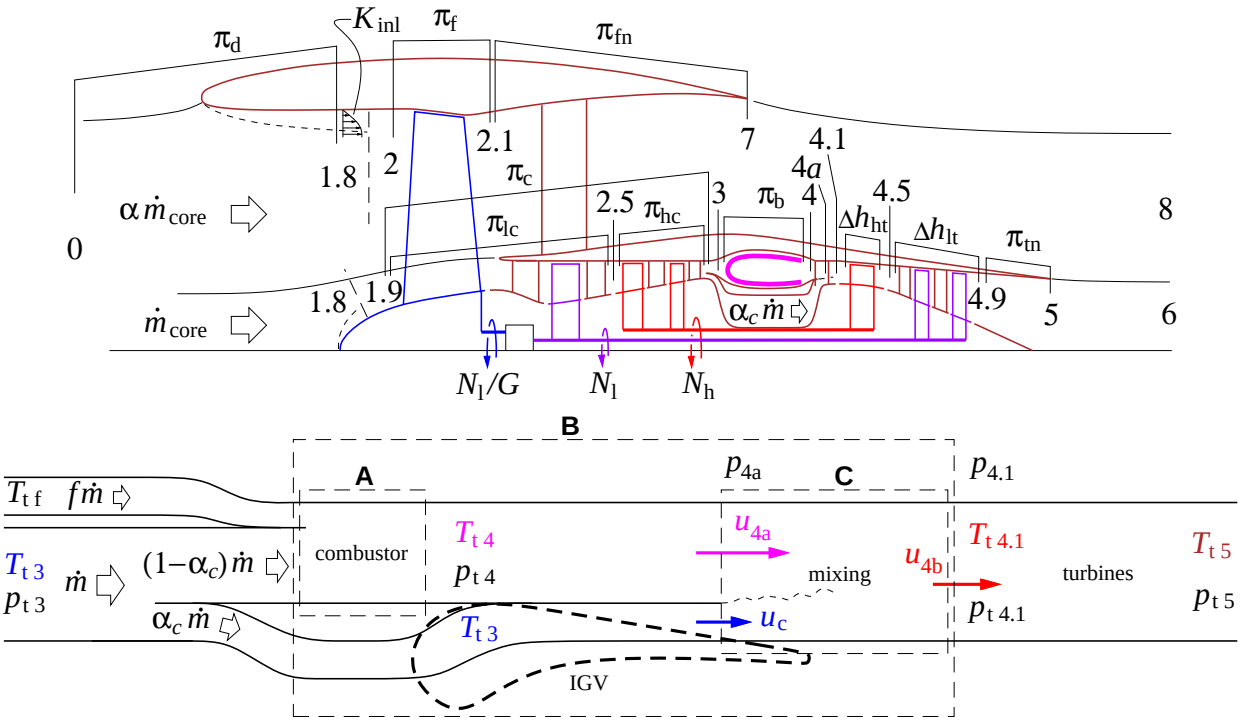

Figure 12: Engine layout used in the turbofan performance model. Gas state variables are computed at all the numbered stations. Bottom figure shows the turbine film-cooling sub-model.

This component-based engine simulation entirely dispenses with the need for engine performance curve fits and correlations. This is deemed especially important for examining designs with extreme engine parameters which fall outside of historical databases, particularly if BLI is also used. The detailed turbine cooling flow model is also essential here, since cooling losses strongly

influence optimum engine variables such as T_{t4}, *FPR*, and *BPR*. The inclusion of the cooling model therefore allows optimization of these engine variables simultaneously with the airframe, aerodynamic, and mission variables, so that a global optimum can be determined.

5 Stability and trim

Each of the weight items shown in Fig. 2 has an associated mass centroid defined, so that a weight-moment buildup can be done in parallel with the weight buildup. Likewise, the spanwise lift integration for the wing and horizontal tail is performed in parallel with a pitching moment integration, including airfoil profile moment contributions. The pitching moment of the fuselage is also added, using a moment coefficient determined via slender body theory and calibrated with off-line vortex lattice calculations for the whole configuration.

The overall weight and aerodynamic moment coefficients C_{M_W}, C_M are then used to impose two conditions: one for pitch trim and one for pitch stability, at the two extreme CG limits chosen among all possible payload and fuel load fraction and distribution situations.

$$\begin{aligned} C_{M_W}(x_{\text{wbox}}) + C_M(C_L, C_{L_\text{h}}, S_\text{h}/S, x_{\text{wbox}}, \ldots) &= 0 \qquad \text{(imposed at most-forward CG)} \\ \frac{\partial C_M}{\partial C_L} + S.M. &= 0 \qquad \text{(imposed at most-rearward CG)} \end{aligned}$$

At each aircraft sizing iteration these two equations implicitly determine two design variables: the wing box location x_{wbox} shown in Fig. 3, and the horizontal tail area S_h. The most-negative allowable horizontal-tail C_{L_h} and the static margin $S.M.$ are specified in this calculation. This procedure ensures that any aircraft which is produced by TASOPT is automatically both pitch-trimmable and stable to within the specified margins.

6 Mission profiles

6.1 Profile calculation

The various quantities from the weight, aerodynamic, and engine models are used in the integration of standard trajectory ODE's over the range flown R, thus determining the weight, altitude, and thrust profiles over the specified mission.

$$\frac{dW}{dR} = -F_\text{eng}\,\frac{TSFC}{V\,\cos\gamma} \tag{10}$$

$$\tan\gamma = \frac{dh}{dR} = \frac{F_\text{eng}}{W}\frac{1}{\cos\gamma} - \frac{C_D}{C_L} - \frac{1}{2g}\frac{d(V^2)}{dR} \tag{11}$$

These are sketched in Fig. 13 together with a few integration points. The cruise is portion is assumed to be at the ideal cruise-climb angle γ_c so as to maintain the specified cruise Mach number and overall airplane C_L at a specified constant cruise turbine inlet temperature T_{t4}. Higher T_{t4} values are specified over the climb, which then determines the climb trajectory. A constant descent angle is specified, and the resulting required T_{t4} is computed at each descent

point. The integration is repeated with varying initial takeoff fuel until the exact specified range is obtained, thus giving the required mission fuel. The end result is a closed design for the aircraft and engine combination which achieves the specified payload and range mission. Off-design missions can also be "flown" with this sized airframe, allowing the possibility of minimizing fuel burn for a collection of fleet missions rather than for just the aircraft-sizing mission.

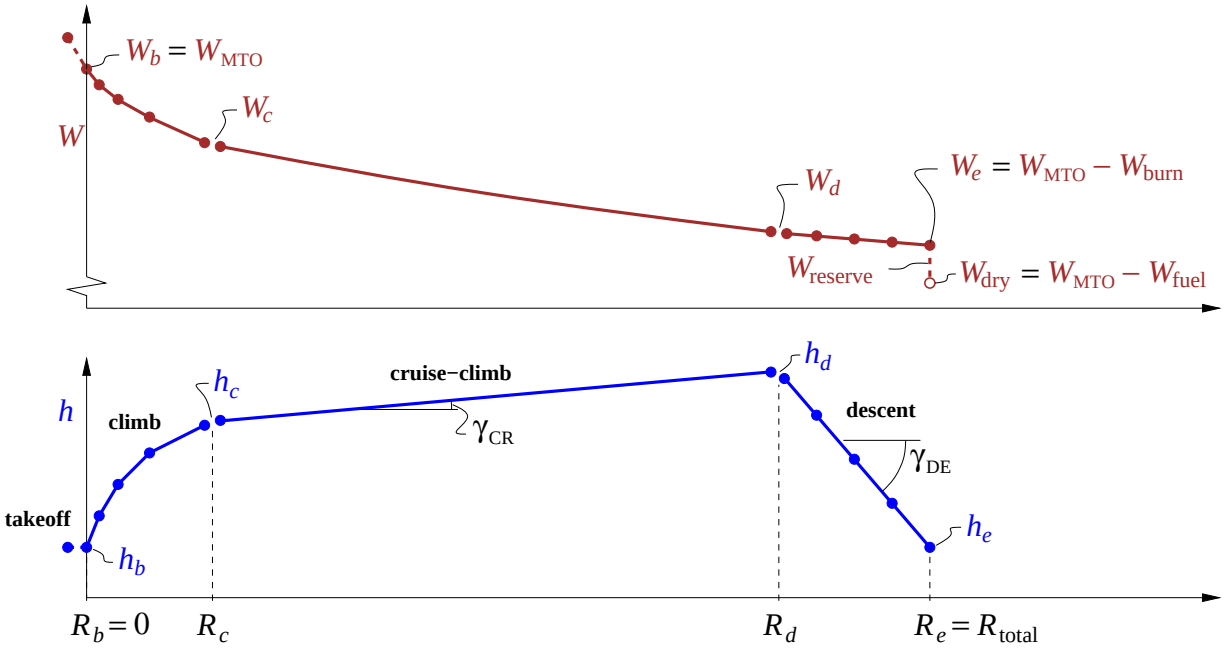

Figure 13: Mission profiles of weight and altitude versus range. Coarse distribution of numerical integration points is shown.

6.2 Takeoff

A takeoff performance model is used to evaluate any given design's balanced field length. This can be optionally included as a constraint in the overall combined airframe + aero + engine + operations optimization, so that the mission fuel-burn penalties of a field-length constraint can be directly evaluated.

7 Weight Iteration and Optimization

TASOPT calculation procedures are organized as nested iteration loops, sketched in Fig. 14 and described below.

7.1 Inner weight iteration loop (design closure)

TASOPT's innermost loop in Fig. 14 applies all the physical models described previously to compute the wing and tail dimensions, the loads and structural gauges, the aerodynamic per-

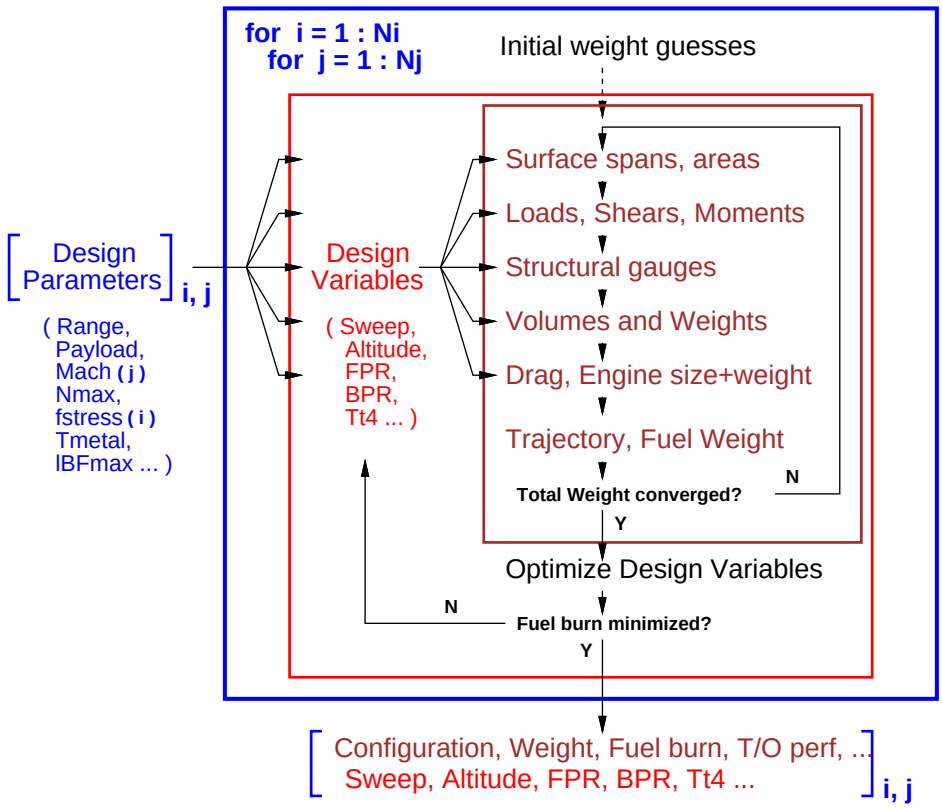

Figure 14: TASOPT organization and data flow. Innermost loop closes any specified design. Middle loop iterates on design variables to minimize fuel burn with constraints. Outer loop sweeps over independent design parameters.

formance, the engine size and performance, the mission fuel, components weights, and the gross takeoff weight. Because the models also require various weights as inputs, the procedure is necessarily iterative.

7.2 Middle design-variable loop (optimization)

The inner design-closure weight iteration loop can optionally be nested in an optimization procedure. A chosen subset (the Design Variables) of the inner-loop inputs are adjusted so that fuel weight is minimized, possibly subject to fuel-volume, balanced field length, or span constraints. All the available design variables are listed in Table 2, but only a partial set can be chosen if appropriate.

7.3 Outer parameter-sampling loop (parameter sweeps)

The inner and middle loops can optionally be nested in an outer parameter-sampling loop over one or more Design Parameters. This simply automates parameter-sensitivity study calculations.

Table 2: List of Design Variables selectable for optimization

$C_{L_{\rm CR}}$	cruise lift coefficient
AR	overall aspect ratio
Λ	wing sweep angle
$(t/c)_o$	airfoil thickness at η_o (wing root)
$(t/c)_s$	airfoil thickness at η_s (planform break or strut-attach)
λ_s	inner panel taper ratio
λ_t	outer panel taper ratio
$r_{c_{\ell_s}}$	clean-configuration c_l/C_L at η_s (planform break)
$r_{c_{\ell_t}}$	clean-configuration c_l/C_L at 1 (tip)
$OPR_{\rm D}$	design overall pressure ratio
$FPR_{\rm D}$	design fan pressure ratio
$BPR_{\rm D}$	design bypass ratio
$h_{\rm CR}$	start-of cruise altitude
$T_{t\,4_{\rm CR}}$	cruise turbine inlet temperature
$T_{t\,4_{\rm TO}}$	takeoff turbine inlet temperature

8 TASOPT Applications

To gain confidence in the TASOPT models and methodology, it was first used to "design" the Boeing 737-800, both with and without optimization. The specified mission is a payload of 38500 lb (180 passengers in single class) over a range of 3000 nautical miles. Also specified are typical load factors, aluminum material properties, and the CFM56-7 engine parameters. TASOPT was then executed for two separate calculations:

1) In a sizing-only mode (inner loop in Fig. 14), with the aspect ratio, sweep, taper ratio, airfoil thickness, cruise C_L and altitude all specified to the 737's values. TASOPT then sized the engine fan diameter, the wing area and span, all the structural gauges and weights, fuel weight, and thus determined the gross weight.

2) In a partial-optimization mode (middle loop in Fig. 14), with the engine variables fixed, and the airframe and aerodynamic variables optimized to minimize the fuel burn.

The results of the two calculations are summarized in Table 3, and the two aircraft are sketched in Fig. 15. It is reassuring that the overall size, fuel burn, and the overall and component weights of the TASOPT-sized airframe match that of the actual airframe reasonably closely. It's also reassuring that the aircraft did not change much during the optimization, since Boeing presumably optimized the 737's design by more traditional techniques.

8.1 Importance of Global Optimization

To investigate the possibility of fuel-burn reduction from reduced cruise Mach and to confirm the effectiveness of global optimization, the B737-800 has been redesigned by TASOPT over the range of cruise Mach numbers $M_{\rm CR} = 0.7 \ldots 0.8$ (the 737's actual maximum cruise Mach is $M_{\rm CR} \simeq 0.79$). The calculation was performed in five Mach sequences, with increasingly more

Table 3: Boeing 737-800 Sizing and Airframe+Ops Optimization (fixed engine)

	W_{MTO} lb	W_{fuel} lb	S ft^2	Λ° deg	λ_t	AR	$C_{L_{\text{CR}}}$	h_{CR} ft
Actual	171000	39000	1230	25.00	0.250	10.20	0.550	33500
1) Sized only	166001	38474	1229	25.00	0.250	10.20	0.550	33500
2) Optimized	163862	36923	1289	24.33	0.144	10.61	0.530	34070

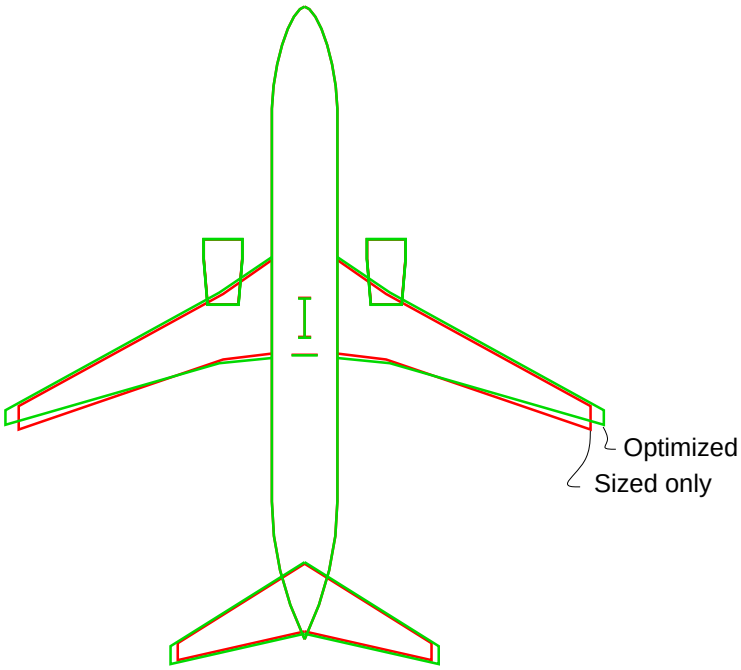

Figure 15: Boeing 737-800 wing and tail geometry calculated by TASOPT, with and without optimization. All primary structural gauges are also calculated.

variables being enabled for optimization at each Mach sequence. The results are summarized in Fig. 16. In lieu of fuel burn, the equivalent but more convenient *PFEI* metric is shown.

$$PFEI \equiv \frac{\text{fuel heat energy expended}}{\text{payload} \times \text{distance flown}} \left[\frac{\text{kJ}}{\text{kg-km}}\right] \tag{12}$$

The main observations are:

- Appropriate design optimization is essential to realize the potential fuel savings of reduced speed. Simply slowing down an airplane with fixed parameters actually increases fuel burn.
- Multi-discipline optimization considerably increases the fuel savings compared to single-discipline optimization.

8.2 Parameter Sensitivity Studies

Fig. 17 shows the results of varying two design parameters: the cruise Mach $M_{\text{CR}} = (0.65 \ldots 0.80)$, and the material allowable-stress multiplier $f_{\text{stress}} = (1.0, 1.25, 1.5)$. The latter is a measure of

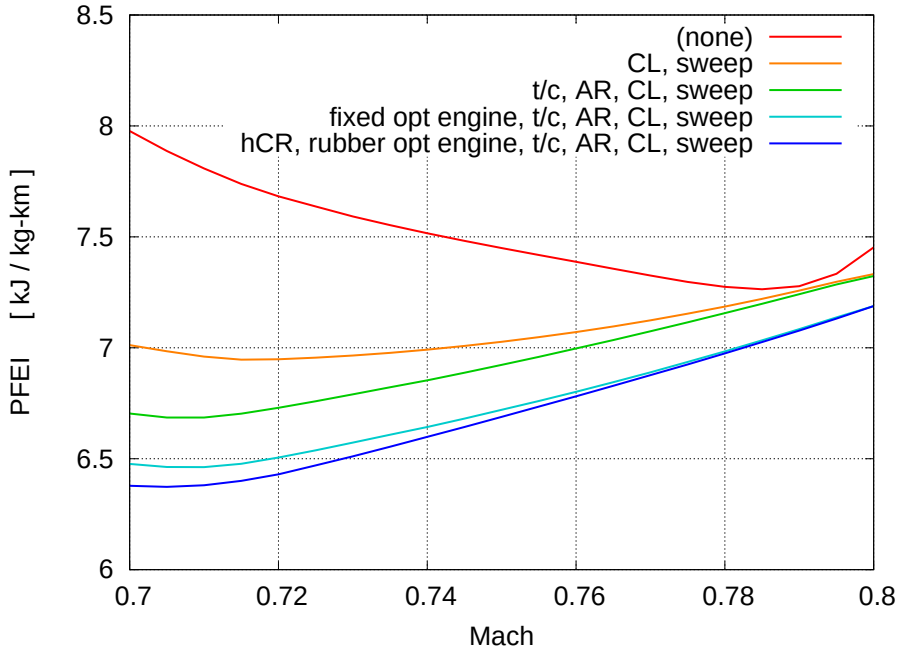

Figure 16: *PFEI* versus cruise Mach number for 737-800–type configuration and mission, for different degrees of optimization. The variables which were optimized for each line are indicated in the legend.

materials technology, with standard aluminum allowables corresponding to $f_{\text{stress}} = 1$.

It should be noted that every point in this parameter space is a different aircraft optimized for that point. A fixed B737-800 fuselage shape is assumed, but its structural gauges vary with the weight and loads. The wing, tail, engine, and flight-profile variables all change as well. The following observations are made:

- Substantial fuel savings result from a decrease in the cruise Mach number down to about 0.72, provided the entire aircraft is re-optimized for the lower speed. Simply slowing down a mostly-stock 737 does not produce any savings, and in fact increases the fuel burn, as can also be seen in Fig. 16.

- Improved materials produce changes in all the optimum variables from other disiplines, which can or should be implemented for maximum benefit: thinner airfoils, increased C_L, increased bypass ratio, reduced turbine inlet temperature, higher cruise altitude, etc.

- Numerous other side benefits result from improved materials if global optimization is performed: lighter (and hence cheaper) optimum engines, reduced optimum fan and core jet velocities giving reduced noise,

9 D8.x Aircraft

Vortex-Lattice and TASOPT studies of various aircraft configurations have indicated that the traditional layout of the B737-800 is considerably sub-optimal. Exploitation of numerous syn-

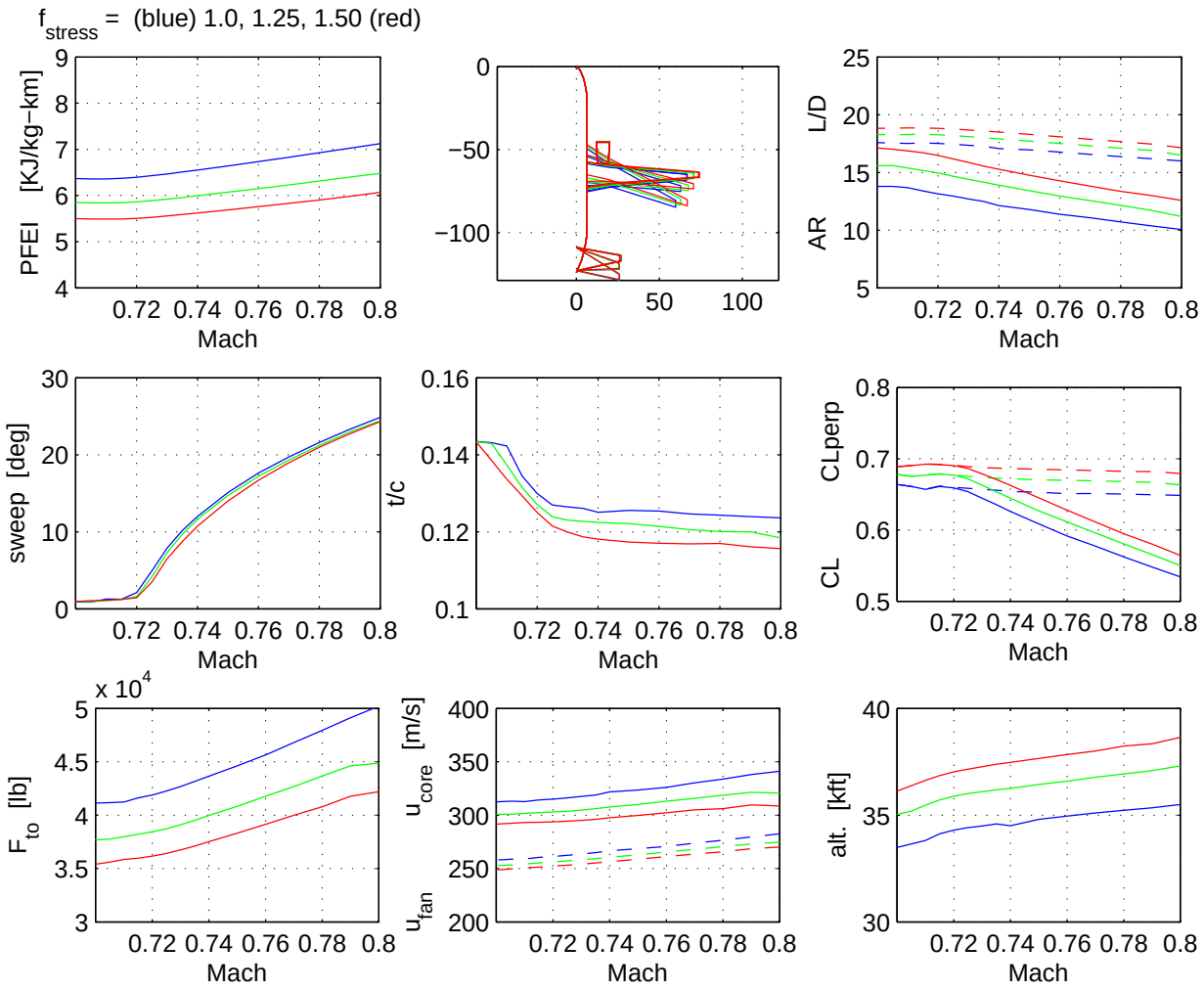

Figure 17: Effects on optimum B737-type aircraft with variation of cruise Mach and material stress factor. Upper left *PFEI* plot is the fuel burn measure.

ergistic effects has resulted in the D8.x configurations. Two basic variants have been developed: The D8.1 which uses today's aluminum technology and engine performance, and the D8.5 which uses advanced composites and engines forecast for year 2030. Table 4 compares the D8.x performance parameters against the Boeing 737-800, all predicted by TASOPT. Again, given that the predicted 737's size, weight, and fuel burn closely match those of the actual airplane gives some confidence in the TASOPT formulation and in the predicted D8.x parameters. The D8.x configurations are compared in Fig. 18, along with a constrained-span variant D8.1b. Fig. 19 shows the D8.1 in much more detail.

A major feature of the D8.x is a reduced Mach number. This is normally undesirable in a transport aircraft, but it is not deemed a serious operational drawback for this relatively short range aircraft. A typical 2500 nmi mission in-flight duration is increased by 25 minutes, which can easily be compensated by faster loading and unloading of the twin aisles relative to the single aisle, so the "door-to-door" trip duration is comparable.

Table 4: Parameter comparison of the 737-800, D8.1b, D8.1, D8.5

	B737-800	D8.1b	D8.1	D8.5
Range	3000 nmi	3000 nmi	3000 nmi	3000 nmi
PAX	180	180	180	180
MTOW	171 000 lb	119 050 lb	133 917 lb	99 756 lb
fuel	39 000 lb	21 650 lb	19 916 lb	11 296 lb
field	7700 ft	5000 ft	5000 ft	5000 ft
Mach	0.79	0.72	0.72	0.74
sweep	25°	6°	5°	13°
area	1230 ft^2	1060 ft^2	1320 ft^2	1142 ft^2
span	112 ft	118 ft	150 ft	168 ft
AR	10.2	13.1	17.3	24.7
d_{fan}	2×63 in	3×46 in	3×48 in	3×52 in
dB_{side}	87.0	81.5	82.0	75.0
dB_{over}	70.5	64.9	65.7	62.3

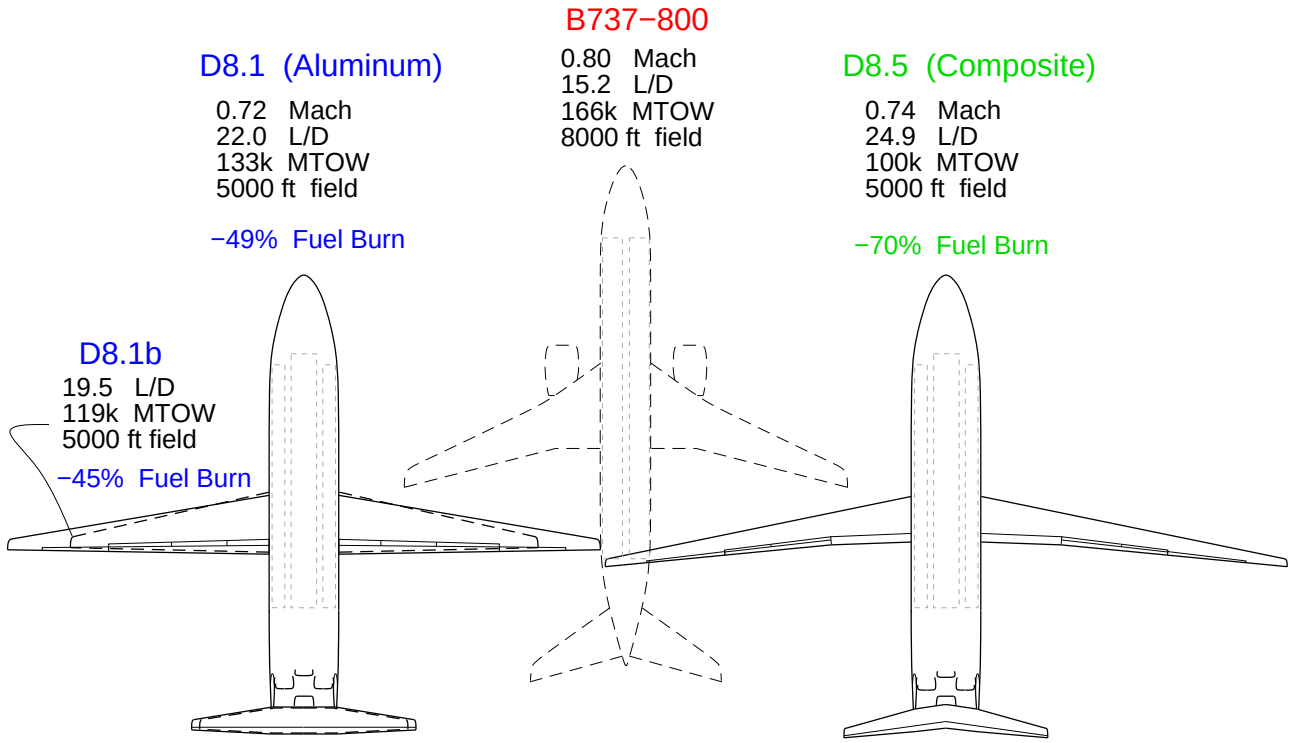

Figure 18: D8.x aircraft compared to Boeing 737-800.

9.1 Breguet analysis

It is useful to examine the D8.x's fuel burn in terms of the Breguet equation, which is simply a special-case analytical solution of the mission trajectory ODE's integrated by TASOPT.

$$W_{\text{fuel}} \;=\; W_{\text{ZF}} \left[\exp\left(\frac{TSFC}{M} \frac{D}{L} \frac{R}{a} \right) - 1 \right] \;\simeq\; W_{\text{ZF}} \frac{TSFC}{M} \frac{D}{L} \frac{R}{a} \tag{13}$$

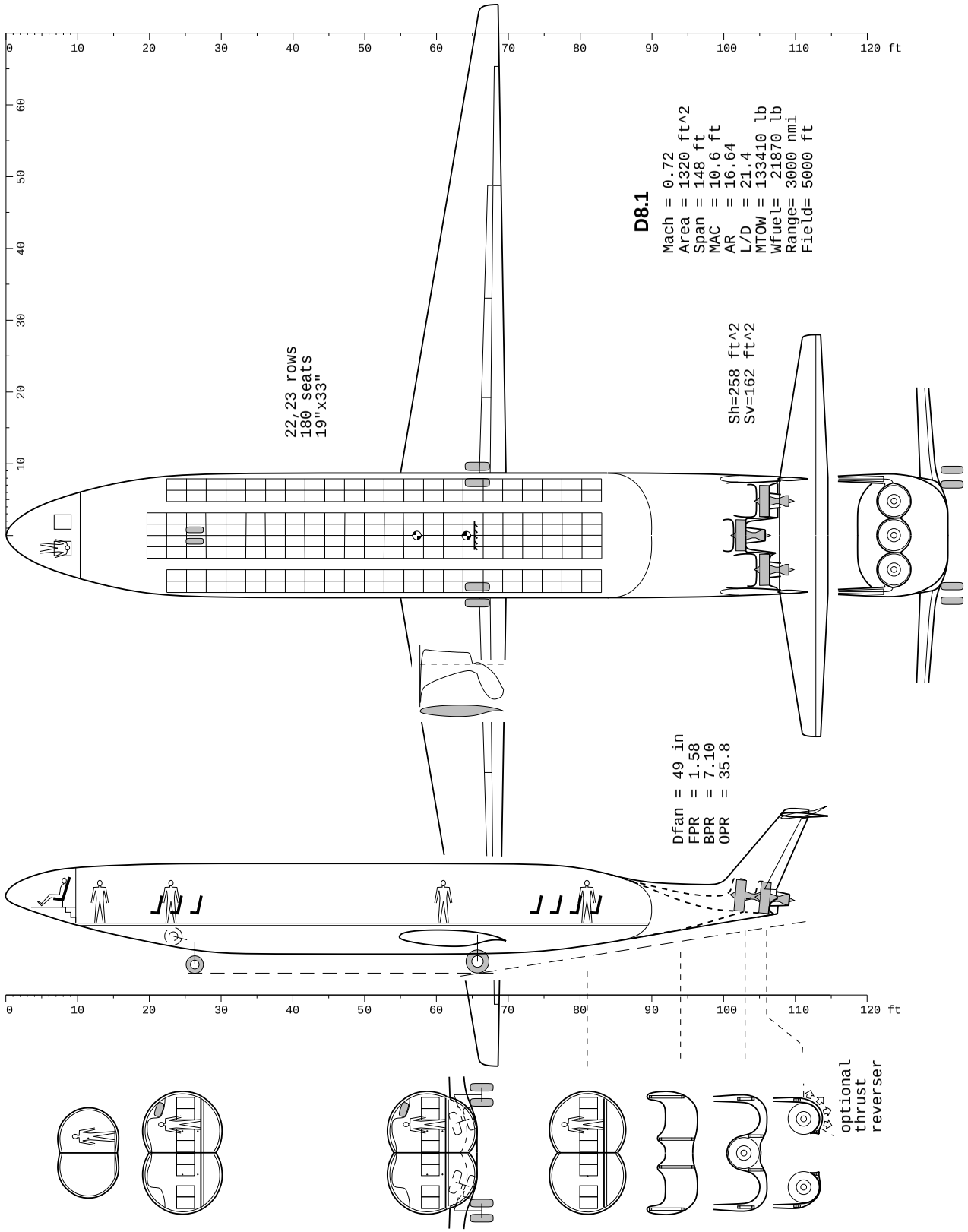

Figure 19: Aluminum-technology D8.1 aircraft.

The second approximate form is valid for the moderate-range 3000 nmi mission, where the exponential nonlinearity is weak. The approximate mission fuel is seen to be a simple product of three terms: the zero-fuel weight W_{ZF}, the engine power-specific fuel burn $TSFC/M$, and the overall D/L ratio. The remaining mission range R and speed of sound a factors are fixed in this case. Fig. 20 compares the three factors for the four airplanes, all normalized to the B737-800 case. The D8.1 improvement is seen to stem most from the D/L improvement, but the weight and engine performance are quite significant as well.

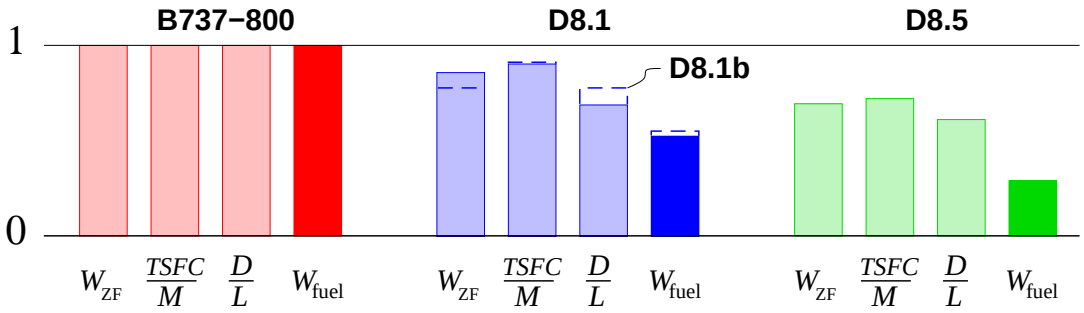

Figure 20: B737-800 and D8.x comparison of fuel burn in terms of Breguet equation parameters, normalized to the B737-800 case. The zero-fuel weight W_{ZF}, engine $TSFC/M$, and D/L all significantly contribute to the overall D8.x improvement.

Fig. 20 is only partly informative in that it does not reveal that the decrease in each of the three terms of the D8.x is the result of synergistic interaction between structures, aerodynamics, and engine characteristics, all captured by TASOPT's models. This synergism would not be fully realized if each of these disciplines were optimized in isolation.

9.2 Features of D8.x aircraft

Below is an itemized list of the features of the D8.x aircraft which produce its large fuel savings relative to the B737-800 baseline via numerous model interactions. These are further illustrated in Figs. 21,22.

- Reduced $M = 0.72$ with unswept wing ...
  - reduced C_{D_i}, via larger AR allowed by unsweep
  - need for LE slat eliminated, via increased $C_{L_{max}}$ from unsweep
  - NLF on wing bottom possible, via unsweep and no slat
  - shorter landing gear
  - smaller difference between cruise Mach and fan-face Mach, reducing nacelle loading, surface velocities, and drag
- Wide double-bubble fuselage with lifting nose
  - increased optimum carryover lift and effective span, via fuselage shape
  - built-in nose-up trimming moment, via fuselage lift on nose region

  - partial span loading via 216" wide fuselage (vs 154")
  - reduced floor-beam weight via center floor support
  - improved propulsive efficiency via fuselage BL Ingestion, enabled by lower cruise Mach to eliminate inlet diffusion and secondary flows into the fan

- Pi-tail unit, with flush-mounted engines
  - improved propulsive efficiency via fuselage BL Ingestion
  - lightweight minimal nacelles, via engine flow alignment by aft fuselage and fins
  - immune to bird strike, since engines are invisible head-on
  - fin strakes synergystically exploited:
    * function as pylons carrying engine loads and tail surface loads
    * shield fan faces from ground observers
  - small vertical tails, via small engine-out yaw moments
  - no typical weight penalty of T-tail, via twin Pi-tail fins
  - lightweight horizontal tail, via its two-point mounting

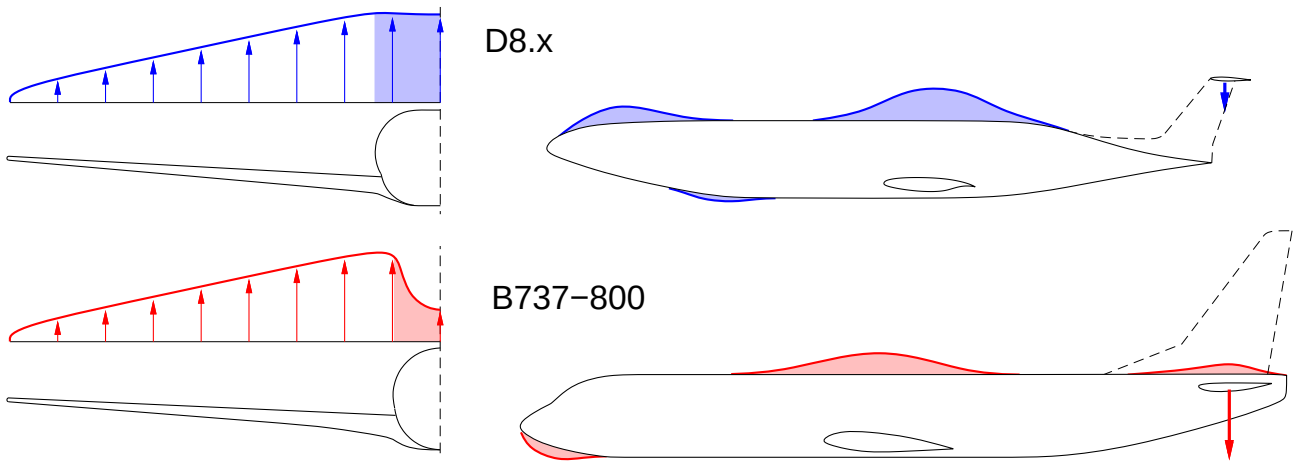

Figure 21: B737 and D8.x comparison of spanwise lift distribution. For D8.x, the fuselage carryover portion is significantly larger (which shrinks the wing), and also distributed to produce a nose-up moment (which shrinks the tail).

10 Summary

This paper has presented the TASOPT method for transport aircraft preliminary design and optimization, which uses a collection of low-order models for the primary structure, aerodynamics, and engine performance. The models are physics-based and do not rely on historical correlations, giving confidence in their application to novel aircraft parameter combinations and configurations. Applications include sensitvity studies to technology improvement accounting for all interactions between disciplines. Also presented is the B737-800 replacement D8.x series of aircraft, which show extremely large fuel burn reductions, even with today's technology.

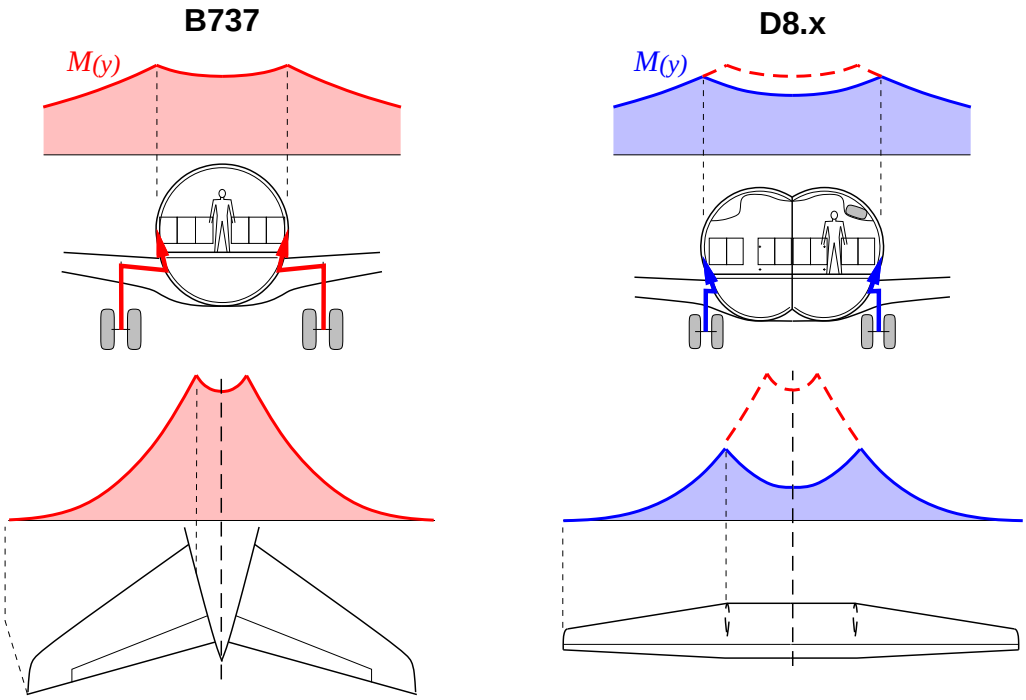

Figure 22: B737 and D8.x comparison of landing gear load path, wing bending moment, and tail bending moment. D8.x wide fuselage and 2-point tail support reduces weight for all components.

References

[1] J. Roskam. *Airplane Design*. DAR Corporation, Lawrence, Kansas, 2000.

[2] E. Torrenbeek. *Synthesis of Subsonic Airplane Design*. Delft University Press, 1988.

[3] D.P. Raymer. *Aircraft Design: A Conceptual Approach*. AIAA Education Series. AIAA, 1992.

[4] S. Jayaram, A. Myklebust, and P. Gelhausen. ACSYNT — A standards-based system for parametric computer aided conceptual design of aircraft. AIAA Paper 92-1268, Feb 1992.

[5] W.H. Mason and T.K. Arledge. ACSYNT aerodynamic estimation — An examination and validation for use in conceptual design. AIAA Paper 93-0973, Feb 1993.

[6] B. Knapp, Matt. Applications of a nonlinear wing planform design program. Master's thesis, MIT, Aug 1996.

[7] S. Wakayama. *Lifting Surface Design Using Multidisciplinary Optimization*. PhD thesis, Stanford, June 1994.

[8] S. Wakayama. Blended-wing-body optimization setup. AIAA Paper 00-4740, Sept 2000.

[9] I. Kroo. PASS, program for aircraft synthesis studies. Software Package, Desktop Aeronautics, Palo Alto, CA, 2005.

[10] J.R.R.A. Martins, J.J. Alonso, and J.J. Reuther. Complete configuration asero-structural optimization using a coupled sensitivity analysis method. AIAA Paper 02-5402, Sept 2002.

[11] M. Drela. Power balance in aerodynamic flows. *AIAA Journal*, 47(7):1761–1771, July 2009. Also AIAA Paper 09-3762, San Antonio Conference, June 2009.

[12] M. Drela and M.B. Giles. Viscous-inviscid analysis of transonic and low Reynolds number airfoils. *AIAA Journal*, 25(10):1347–1355, Oct 1987.

[13] M. Drela. XFOIL: An analysis and design system for low Reynolds number airfoils. In T.J. Mueller, editor, *Low Reynolds Number Aerodynamics*. Springer-Verlag, Jun 1989. Lecture Notes in Engineering, No. 54, http://raphael.mit.edu/xfoil/.

[14] J.L. Kerrebrock. *Aircraft Engines and Gas Turbines, 2nd Ed.* The MIT Press, Cambridge, 1996.